数理解析研究所講究録 第2109巻 2019年 21-32

Numerical Simulations of Baroclinic Tide Fields in the Global Ocean: Estimation of Baroclinic Tide Energy Available for Deep Ocean Mixing

Yoshihiro Niwa

UTokyo Alliance, The University of Tokyo,
7-3-1 Hongo, Bunkyo-ku, Tokyo, 113-0033 Japan

Abstract

The global distributions of the major semidiurnal (M_2 and S_2) and diurnal (K_1 and O_1) baroclinic tide energy are investigated using a hydrostatic numerical model. A series of numerical simulations using various horizontal grid spacing of Δx=1/5˚-1/20˚ shows that generation of energetic baroclinic tides is restricted over prominent topographic features. It is also found that the energy conversion rate from barotropic to baroclinic tide is very sensitive to horizontal grid spacing as well as the resolution of the model bottom topography. Extrapolating the calculated results to the limit of zero horizontal grid spacing (Δx=0˚) yields the estimate of the global baroclinic conversion rate to be 1240 GW. The amount of baroclinic tide energy dissipated in the open ocean below a depth of 1000m (the typical depth of the main thermocline) is estimated to be 560-680 GW, which is comparable to the mixing energy estimated by Webb and Sughinohara (2001) as needed to sustain the global thermohaline circulation.

1. Introduction

Baroclinic tides are ubiquitous phenomena in the stratified ocean. They are generated by barotropic tidal currents flowing over a rough ocean bottom such as mid-ocean ridges and continental shelf slopes; the stratified water is then vertically displaced up and down and part of the barotropic tide energy is converted into baroclinic tide energy.

Baroclinic tides have a strong influence on the global thermohaline circulation and hence on the world's climate, because they are thought to contribute to turbulent mixing in the deep ocean; near the generation sites, the vertical shear of horizontal currents associated with baroclinic tides can be strong enough to cause shear instability leading to locally enhanced turbulent mixing. Turbulent mixing can also be induced even far from the generation sites, because propagating baroclinic tides nonlinearly interact with the background internal waves and/or mesoscale eddies and cascade part of their energy down to small dissipation scales inducing shear instability. Thus induced turbulent mixing transfers heat from the surface

down to the dense deep water that originates from high latitudes, causing it to upwell back to the sea surface at low and mid latitudes. Actually, ocean general circulation models (e.g., Hasumi and Suginohara 1999) demonstrate that the rate and spatial distribution of turbulent mixing can strongly control the fundamental features of the global thermohaline circulation such as flow and density structures as well as the transport of heat and chemical tracers.

Accurate estimation of baroclinic tide energy is also crucial for understanding the energy balance of the global thermohaline circulation. Munk and Wunsch (1998) estimated that 2100 GW (1 GW $=10^9$ W) of mixing energy is required to pull up 30Sv (1Sv$=10^6 m^3/s$) of the dense deep water below a depth of 1000m (the typical depth of the main thermocline) and postulated that nearly half of that energy was supplied by baroclinic tides and the remaining half by the wind-induced internal waves. On the other hand, Webb and Suginohara (2001) suggested that the direct upwelling by wind stress (Ekman suction) in the Southern Ocean around the Antarctic continent might pull up about half of the deep water formed in the North Atlantic to the sea surface, reducing the required mixing energy to as low as 600 GW. It still remains a matter of debate as to which of these mixing energy analyses is more convincing. An important step toward answering this question is to accurately estimate the amount of baroclinic tide energy available for deep ocean mixing.

In the present study, we investigate the spatial distribution of the major semidiurnal (M_2 and S_2) and diurnal (K_1 and O_1) baroclinic tides using a fine-grid three-dimensional numerical model incorporating realistic bottom topography, density stratification, and barotropic tidal forcing. In order to accurately estimate the energy conversion rate from barotropic tides to baroclinic tides, in particular, a series of numerical simulations with various horizontal grid spacings is conducted to examine the sensitivity of the calculated results to the model grid spacing as well as the resolution of the model bottom topography.

2. Numerical simulations

Fig. 1 shows the model domain that covers the global ocean from 80°S to 80°N. The governing equations are the full three-dimensional Navier–Stokes equations under hydrostatic and Boussinesq approximations. The governing equations are numerically integrated using the Princeton Ocean Model (Blumberg and Mellor, 1987). To examine the sensitivity of the model results to the horizontal grid spacing as well as the resolution of the model bottom topography, a set of numerical experiments is carried out using six different horizontal grid spacings, namely, Δx=1/5°, 1/6°, 2/15°, 1/10°, 1/15°, 1/20°. In all cases, 41 sigma levels are

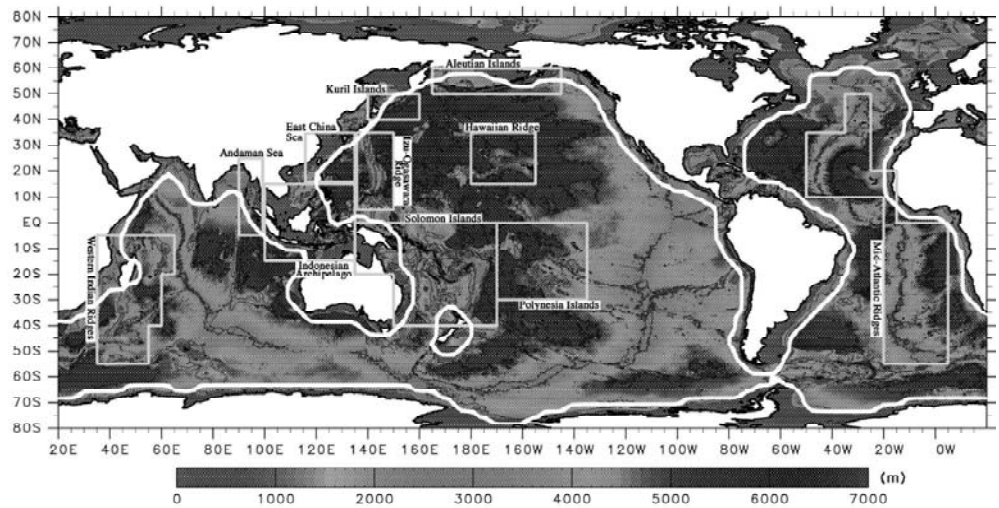

Fig. 1. The whole model domain and the bathymetry. The regions including the prominent topographic features are indicated by straight lined squares. The thick white line indicates the boundary between the open ocean and the coastal and marginal seas.

assumed in the vertical. For details of the governing equations and the numerical model, readers are referred to Niwa and Hibiya (2004).

For each numerical experiment, the model topography is constructed by averaging the 1-min (1/60°) gridded global bathymetric data of ETOPO1 within each model grid cell so as to increase the resolution of the model topography with the decrease of the model grid spacing. The basic temperature and salinity fields are obtained from the annual mean data of the National Oceanographic Data Center's World Ocean Atlas. The model is forced by the tidal potential forcing of four major semidiurnal and diurnal astronomical tidal constituents (M_2, S_2, K_1 and O_1). The time periods of M_2, S_2, K_1 and O_1 tidal forcing are 12.42hrs, 12.00hrs, 23.93hrs and 25.82hrs, respectively. Furthermore, in order to reproduce the realistic barotropic tidal field, we assimilate the barotropic surface tidal elevation data from the tidal prediction system of NAO.99b (Matsumoto et al., 2000). The model is driven by the M_2, S_2, K_1 and O_1 tidal forcing for 60 days from an initial state of rest with time steps of 30s and 3.75s for the baroclinic and barotropic modes, respectively. The calculated time series data for the last 20 days are harmonically analyzed to obtain the amplitude and phase of each tidal constituent. In order to extract the information about baroclinic tides, we subtract the depth-averaged tidal currents from the calculated tidal currents.

3. Results

Figs. 2a and 2b show the snapshot of vertical displacement at the depth of 1000m in the mid-latitude North-Western Pacific for semidiurnal (M_2 and S_2) and diurnal (K_1 and O_1) baroclinic tides, respectively. The characteristic horizontal wavelength becomes ~150km for semidiurnal baroclinic tides and ~300km for diurnal baroclinic tides. Energetic baroclinic tides with an amplitude up to several tens meters are excited over the Luzon ridge located between Taiwan and the Philippines and over the Izu-Ogasawara ridge.

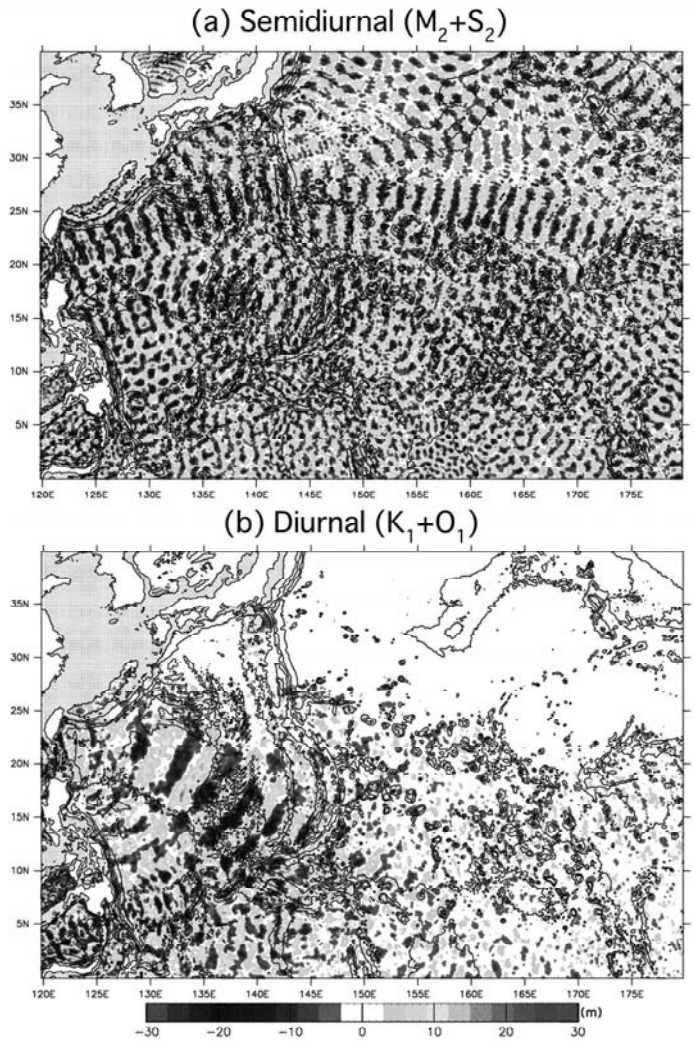

Fig. 2. (a) The snapshot of vertical displacement field for semidiurnal (M_2 and S_2) baroclinic tides at depth 100m in the mid-latitude North Western Pacific. (b) same as (a) but for diurnal (K_1 and O_1) baroclinic tides.

Fig. 2b shows that the propagation of diurnal baroclinic tides is limited equatorward of the latitude about 30˚. This is because frequency of freely propagating linear internal waves must be greater than the Coriolis frequency f ($f = 2\Omega\sin\theta$ where Ω=1/24hrs^{-1} is the earth's rotation frequency and θ is latitude), hence the diurnal baroclinic tides cannot propagate freely poleward of the critical latitude of about 30˚ where the diurnal tidal frequency becomes equal to the Coriolis frequency (the exact critical latitudes for K_1 and O_1 baroclinic tides are 30.01˚ and 27.69˚, respectively).

To examine the generation of baroclinic tide energy more quantitatively, we calculate the depth-integrated energy conversion rate from the barotropic to baroclinic tides (Niwa and Hibiya, 2004) defined as,

$$CNV(x,y) = \int_{-H}^{0} g\overline{\rho' W_{bt}}\, dz$$

where H is the depth, g is the gravity acceleration, ρ' is the density deviation from the basic density field due to baroclinic tide motions, W_{bt} is the vertical velocity resulting from the interaction of depth-averaged tidal currents with bottom topographies and the overbar denotes the temporal average over one tidal period.

The baroclinic tidal energy conversion rate integrated over the global ocean ($\iint_{global} CNV(x,y)dxdy$) amounts to 914 GW (673, 117, 83, 41 GW for M_2, S_2, K_1, and O_1 constituents, respectively) for the case of the finest horizontal grid spacing Δx= 1/20˚. However, the calculated baroclinic conversion rate is very sensitive to the choice of the horizontal grid spacing (Δx). Fig. 3 plots the globally integrated baroclinic conversion rates obtained for each numerical simulation versus the horizontal grid spacing (Δx). The global baroclinic conversion rate for the sum of M_2, S_2, K_1 and O_1 tidal constituents increases by 512 GW (from 393 GW to 912 GW) as Δx is reduced from 1/5˚ to 1/20˚. This significant increase of the global baroclinic conversion rate is primarily attributable to the increase of the spatial resolution of the model bottom topography rather than the improvement of the model grid resolution itself. Actually, when Δx is reduced from 1/5˚ to 1/20˚ but with fixing the model topography resolution (i.e. the topography smoothed with averaging scale of 1/5˚ is used in both calculations), the increase of the global baroclinic conversion rate is limited to 167 GW (from 393 GW to 560 GW).

Fig. 3 indicates that the logarithm of the global baroclinic conversion rate increases almost linearly with the decrease of Δx. Hence, we extrapolate the least-squares fitting in Fig. 3 to

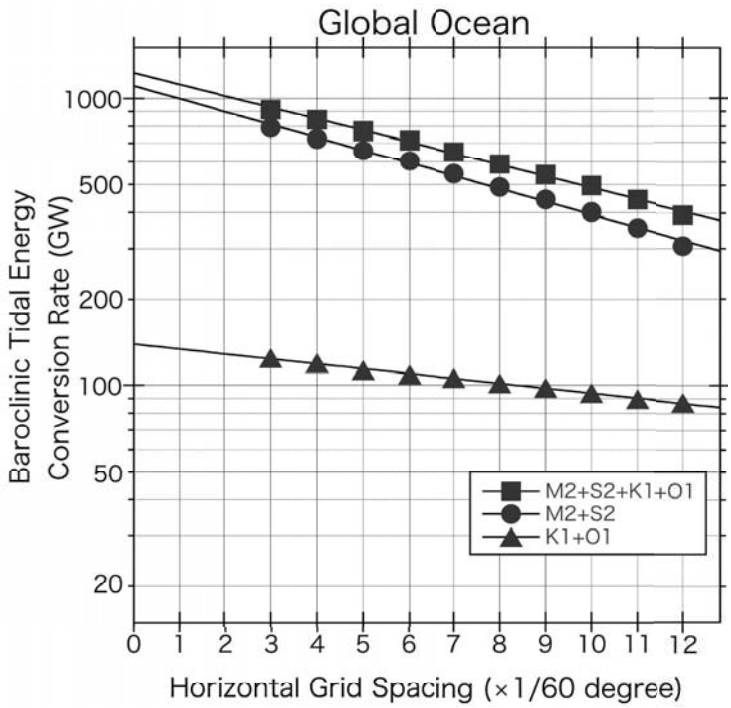

Fig. 3. The globally integrated baroclinic tidal energy conversion rates for the semidiurnal (solid circles) and diurnal tidal constituents (solid triangles) and the sum of the four major tidal constituents (solid squares) obtained using various horizontal grid spacing of 1/20°–1/5°. Superposed on each plot is the least squares fitting line.

the limit of zero grid spacing ($\Delta x = 0^{\circ}$) to estimate the global baroclinic conversion rate to be 1238 ± 35 GW (937 ± 35, 163 ± 3, 92 ± 4, 46 ± 3 GW for M_2, S_2, K_1 and O_1 tidal constituents, respectively). Since the global barotropic tidal energy input from the astronomical tidal potential forcing amounts to 3500 GW (Munk and Wunsch, 1998), the above estimate indicates that 35% of the total barotropic tidal energy is converted to baroclinic tidal energy.

To examine the locations where the baroclinic tide energy is generated, the global distribution of the baroclinic tidal energy conversion rate for the sum of M_2, S_2, K_1 and O_1 tidal constituents is shown in Fig.4, which is averaged over each $5^{\circ} \times 5^{\circ}$ grid area. Note that Fig.4 shows the baroclinic conversion rate estimated by the extrapolation to the limit of $\Delta x = 0^{\circ}$. The details of the extrapolation are explained in Niwa and Hibiya (2014). We can see that the generation of energetic baroclinic tides is concentrated in several specified regions.

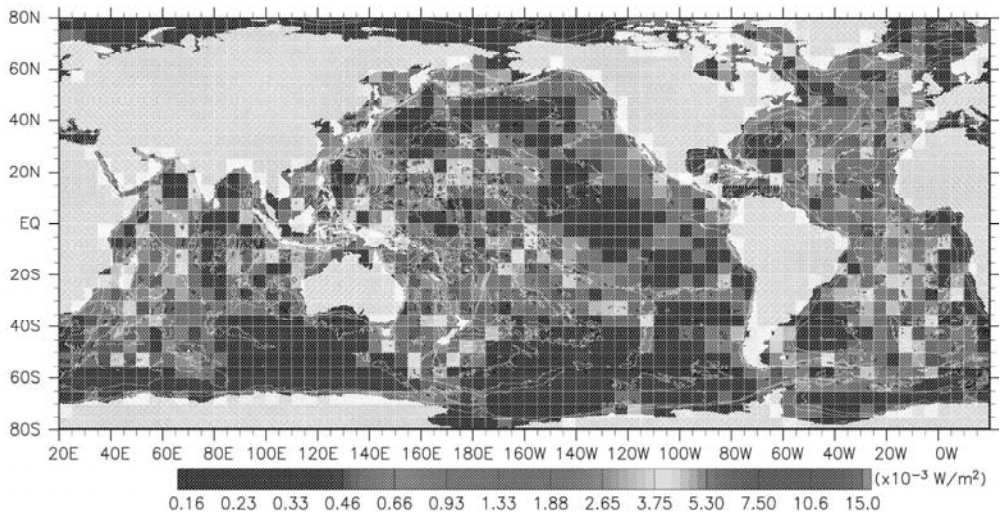

Fig.4. The global distribution of the baroclinic tidal energy conversion rates for the sum of the four major tidal constituents (M_2, S_2, K_1 and O_1) averaged within each $5^\circ \times 5^\circ$ grid area. The baroclinic conversion rate estimated in the limit of zero horizontal grid spacing ($\Delta x = 0^\circ$) is shown.

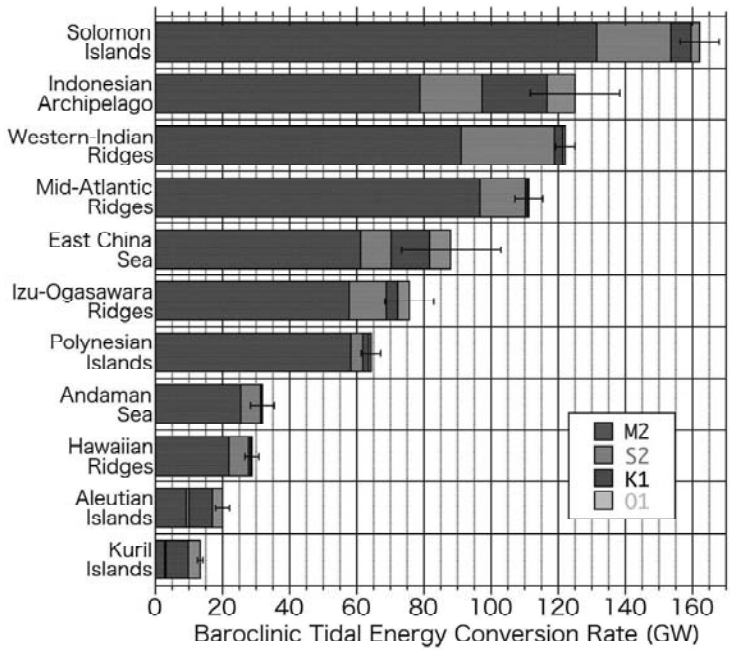

Fig.5. The integrated semidiurnal (M_2, S_2) and diurnal (K_1, O_1) baroclinic tidal energy conversion rates over each representative area (see Fig. 1) estimated in the limit of zero grid spacing ($\Delta x = 0^\circ$).

Fig.5 shows the baroclinic conversion rate integrated over each of the significant generation regions indicated in Fig.1 with the squares enclosed by straight lines. Over these significant regions, about 70% of the globally integrated baroclinic tide energy is generated. Especially, the Solomon Islands, the Indonesian Archipelago, the Western Indian Ridges, and the Mid-Atlantic Ridges are the four most important generation regions, over which more than 100 GW of baroclinic tide energy is generated.

Next, in order to estimate how much of the baroclinic tide energy is dissipated in the open ocean below a depth of 1000m (the typical depth of the main thermocline) to induce the deep-ocean mixing that sustains the thermohaline circulation, we first calculate the depth-integrated dissipation rate of baroclinic tide energy. Assuming nonlinear advection effect is negligible, it is given by the difference between the energy conversion rate and the energy flux divergence,

$$DIS(x,y) = \int_{-H}^{0} g\overline{\rho' W_{bt}}\, dz - \int_{-H}^{0} \left[\frac{\partial}{\partial x}(\overline{p'u'}) + \frac{\partial}{\partial y}(\overline{p'v'})\right] dz$$

where u', v' and p' are the eastward and northward velocities and the pressure perturbations associated with baroclinic tide motions, respectively. The spatial distribution of $DIS(x,y)$ (not shown here) is similar to that of $CNV(x,y)$ shown in Fig. 4, but extends more outward from each prominent topographic feature as a consequence of baroclinic tide propagation. If the boundary between the open ocean and the coastal and marginal seas is defined as shown by the thick white line in Fig. 1, we can estimate the baroclinic dissipation within the open ocean $\iint_{open} DIS(x,y)dxdy$ to be 833 ± 23 GW (405 ± 11 GW for the coastal and marginal seas) in the limit of $\Delta x = 0^{\circ}$.

Recent turbulence observations have shown that the turbulent dissipation rate associated with breaking of baroclinic tides decays upwards from the ocean bottom ($z = -H$) with a scale height (ς) several tens to hundreds meters depending on the characteristic wavelength of ocean bottom roughness (Decloedt and Luther, 2010). Taking this into account, we assume that the depth-integrated baroclinic tidal energy dissipation rate $D(x,y)$ is vertically distributed following a vertical structure function given by

$$\phi(z;H) = \frac{e^{-(z+H)/\varsigma}}{\varsigma(1 - e^{-H/\varsigma})}$$

which satisfies $\int_{-H}^{0} \phi(z;H)dz = 1$. Then, the fraction of the baroclinic tide energy that is dissipated in the open ocean at depths greater than $|z|$ can be calculated as

$$F_{open}(z) = \frac{\iint_{open}\left[\int_{-H(x,y)}^{z} DIS(x,y)\phi(z';H(x,y))\,dz'\right]dxdy}{\iint_{Global} CNV(x,y)dxdy}.$$

Fig. 6 shows the plots of $F_{open}(z)$ (thick solid lines) for the scale height parameters ς= 10, 100, 500, 1000 m, respectively. The same function but for the coastal and marginal seas is $F_{coastal}(z)$ is also plotted in Fig. 6 (thin dotted line). Although the value of $F_{open}(z)$ at each z decreases as the scale height parameter ς increases, $F_{open}(z)$ does not change appreciably even if ς is varied over two orders of magnitude. Fig. 6 indicates that 45–55% of the global baroclinic tide energy is dissipated in the open ocean below the depth of 1000 m ($F_{open}(|z| = 1000m)$). Multiplying this fraction by the global energy conversion rate estimated in the limit of zero horizontal grid spacing (about 1240GW), we can estimate that 560–680 GW of the baroclinic tide energy is supplied to the deep ocean mixing which is available to sustain the global overturning circulation.

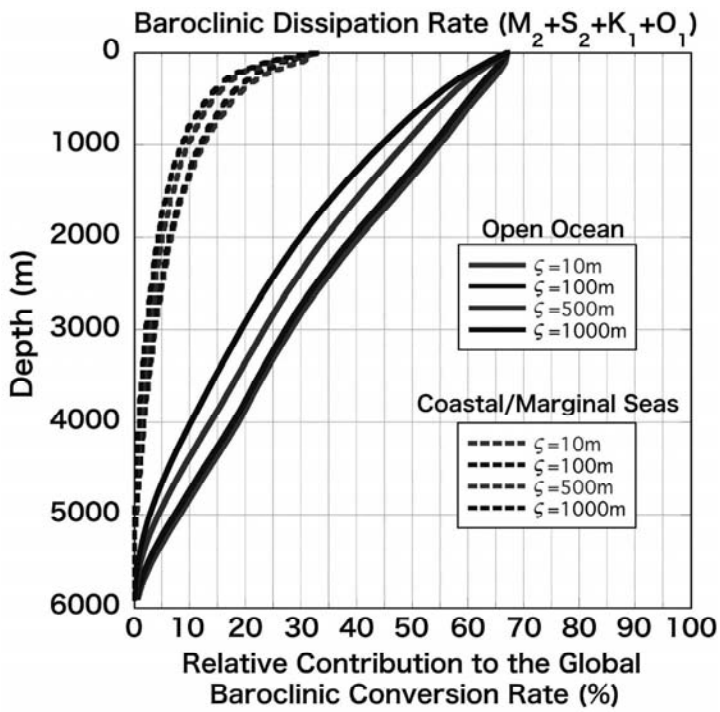

Fig. 6. The cumulative depth distribution of the dissipation rate of baroclinic tide energy for the four major tidal constituents (M_2, S_2, K_1, and O_1) within the open ocean (solid lines) and within the coastal and marginal seas (dotted lines) which are calculated assuming an exponential vertical structure function with various scale height parameters ς = 10, 100, 500, and 1000 m.

3. Summary and Discussion

In the present study, using a three-dimensional numerical model, we have investigated the global distribution and budget of the semidiurnal and diurnal (M_2, S_2, K_1, and O_1) baroclinic tide energy. The sensitivity experiments have shown that the energy conversion rate from the barotropic to baroclinic tides strongly depends on the horizontal grid spacing (Δx) as well as the resolution of the model bottom topography; the energy conversion rate increases exponentially as Δx is reduced from 1/5° to 1/20°.

This clearly indicates the necessity of very high resolution numerical simulations (horizontal grid spacing much less than 1/100°) incorporating fine-scale bathymetric data such as those obtained by multibeam echo sounder observations from research ships or ROVs (remotely operated underwater vehicle). However, such very high resolution numerical simulations covering all the global ocean is impossible for the moment because of insufficient computer capacity as well as insufficient spatial coverage of multibeam bathymetric data.

In the present study, we have instead estimated the baroclinic energy conversion rate in the limit of zero horizontal grid spacing ($\Delta x = 0°$) by extrapolating the exponential relationship found between the calculated energy conversion rate and Δx. Fig. 7 shows the global tidal energy budget obtained from the this study. We have found that 3500 GW of the global barotropic tidal energy is converted into 1240 GW of baroclinic tide energy over the prominent topographic features in the global ocean, about 830 GW of which is dissipated within the open ocean. We have also found that 45–55% of the global baroclinic tide energy is dissipated below a depth of 1000 m (the typical depth of the main thermocline) in the open ocean so that 560–680 GW of the baroclinic tide energy is estimated to be available for deep ocean mixing.

This value is just barely 30% of 2100 GW, namely, the energy required to sustain the global overturning circulation estimated by Munk and Wunsch (1998). They have argued that the remaining energy for deep ocean mixing could be supplied by the wind-induced internal waves. However, numerical simulations by Furuichi et al. (2008) demonstrated that the globally integrated wind-induced near-inertial internal wave energy available for deep ocean mixing was limited to 100 GW, because more than 70% of the wind-induced near-inertial wave energy was dissipated within the top 200 m and hence not available for turbulent mixing at greater depths. Even adding the contribution from the wind-induced internal waves, therefore, the estimated total energy available for deep ocean mixing of 660–780 GW is still

much insufficient to fulfill the mixing energy estimated by Munk and Wunsch (1998). This result seems to support the validity of the argument of Webb and Suginohara (2001) who insisted that the required mixing energy can be reduced down to 600 GW by considering the existence of the direct upwelling by wind stress (Ekman suction) in the Southern Ocean that pulls up about half of the North Atlantic Deep Water (NADW) formed in North Atlantic.

Acknowledgements

I would like to thank Prof. Sunao Murashige and the participants to the workshop for giving me the opportunity to present this work and to have useful discussions. Furthermore, I would like to express the deepest respect to Prof. Mitsuhiro Tanaka for his significant achievements in the research of water wave physics and for his dedicated efforts in the promotion and education of this research field.

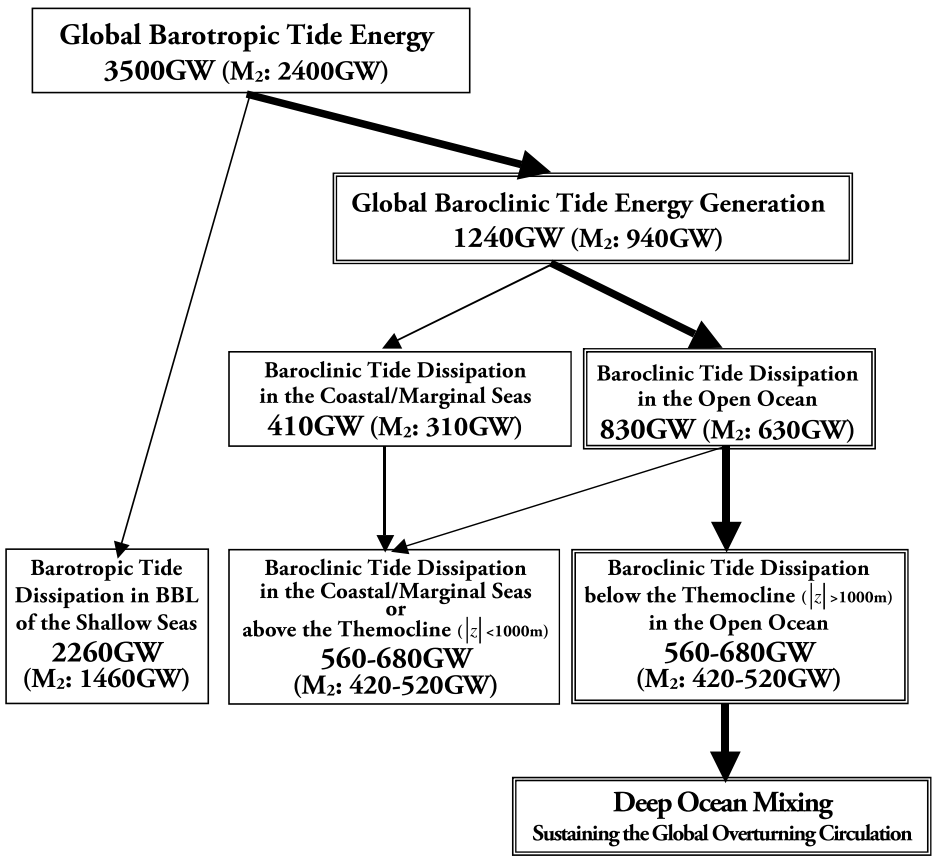

Fig. 7. The global tidal energy budget estimated in the present study

References

Blumberg A.F., Mellor G.L. (1987), A description of a three-dimensional coastal ocean circulation model, In Heaps N. (ed.), *Three-dimensional coastal ocean models*, AGU, Washington D.C..

Decloedt T., Luther D.S. (2010), On a simple empirical parameterization of topography-catalyzed diapycnal mixing in the abyssal ocean, *Journal Physical Oceanography*, **40**, 487–508.

Furuichi N., Hibiya T., Niwa Y. (2008), Model-predicted distribution of wind-induced internal wave energy in the world's oceans, *Journal Geophysical Research*, **113**, doi:10.1029/2008JC004768.

Hasumi H., Suginohara N. (1999), Effects of locally enhanced vertical diffusivity over rough bathymetry on the world ocean circulation, *Journal Geophysical Research,* **104**, 23367–23374.

Matsumoto K., Takanezawa T., Ooe M. (2000), Ocean tide models developed by assimilating Topex/Poseidon altimeter data into hydrodynamical model: a global model and a regional model around Japan, *Journal of Oceanography*, **56**, 567–581.

Munk W.H., Wunsch C. (1998), Abyssal recipes II: energetics of tidal and wind mixing, *Deep Sea Res Part I*, **45**,1977–2010.

Niwa Y., Hibiya T. (2004), Three-dimensional numerical simulation of M_2 internal tides in the East China Sea, *Journal of Geophysical Research*, **109**, DOI: 10.1029/2003JC001923.

Niwa Y., Hibiya T. (2014), Generation of baroclinic tide energy in a global three-dimensional numerical model with different spatial grid resolutions, *Ocean Modelling*, **80**, 59-73, doi :10.1016/j.ocemod.2014.05.003.

Webb D.J., Suginohara N. (2001), Vertical mixing in the ocean, *Nature*, **409**, 37.